Fine study of hierarchical interphase constructed by Boron Nitride and carbon nanotubes in SiC f /SiC composites

Bing Yan, Benhui Fan, Xiaozhong Huang, Zuojuan Du, Yu Liu, Jianling Yue, Jinbo Bai

Fine study of hierarchical interphase constructed by Boron Nitride and carbon nanotubes in SiC_f/SiC composites

Bing Yan[1,2], Benhui Fan[3], Xiaozhong Huang[1,2], Zuojuan Du[1,2], Yu Liu[1,2*], Jianling Yue[1,2*], Jinbo Bai[4]

1 State Key Laboratory of Powder Metallurgy, Powder Metallurgy Research Institute, Central South University, 410083 Changsha, PR China

2 Hunan Key Laboratory of Advanced Fibers and Composites, Central South University, Changsha, Hunan 410083, China

3 Cerema-ENDSUM, 23 avenue de l'Amiral Chauvin, 49136 LES PONTS DE CÉ Cedex – France

4 LMPS-Laboratoire de Mécanique Paris-Saclay, Université Paris-Saclay, CentraleSupélec, ENS Paris-Saclay, CNRS, Gif-sur-Yvette, France

Corresponding author: Y. LIU (yu_liu@csu.edu.cn), J. Yue (jlyue2010@csu.edu.cn);

Abstract

A fine study of the interfacial part in the silicon carbide fiber (SiC_f) reinforced silicon carbide (SiC) composites was conducted by transmission electron microscopy. The boron nitride (BN) and carbon nanotubes (CNTs) were progressively coated on the SiC_f by CVD method to form a hierarchical structure. Three composites with different interfaces, SiC_f-CNTs/SiC, SiC_f@BN/SiC, and SiC_f@BN-CNTs/SiC, were fabricated by Polymer Infiltration and Pyrolysis (PIP) method. The interfaces and microstructures of the three composites were carefully characterized to investigate the improvement mechanism of strength and toughness. The results showed that BN could protect the surface of SiC_f from corrosion and oxidation so that improved the possibility of debonding and pullout. CNTs could avoid the propagation of cracks in the composites so that improved the damage resistance of the matrix. The synergistic reinforcement brought by BN and CNTs interfaces made the SiC_f@BN-CNTs/SiC composites with a tensile fracture strength as high as 359 MPa, with an improvement of 23% compared to that of SiC_f@BN/SiC.

Keywords: SiC_f/SiC; BN; CNTs; TEM; mechanical properties

1 Introduction

Silicon carbide fiber (SiC_f) reinforced silicon carbide-based composites (SiC_f/SiC) are the most promising thermal structural materials for aerospace and aviation applications[1, 2]. Numerous nations have allocated substantial investments to SiC_f/SiC composites through national research programs, with a primary focus on advancing their utilization within the aerospace industry, particularly in the high-temperature sections of jet engines[3, 4, 5]. Harsh operational conditions have necessitated SiC_f/SiC composites to exhibit enhanced properties, including high-temperature resilience, resistance to oxidation, fatigue endurance, and corrosion resistance. The interfacial layer serves as a critical bonding element between the fibers and the matrix in SiC_f/SiC composites. The microstructures of this interface significantly influence the mechanical characteristics of the composites, particularly their toughness[6, 7, 8, 9]. In SiC_f/SiC composites, interfaces have the capacity to hinder crack propagation, transmit loads from the matrix to the fibers, subsequently relieving residual thermal stresses, and offer protective measures during both the preparation and utilization phases[10]. Hence, the design of the interface is essential to obtain SiC_f/SiC composites with further improved performance.

Boron nitride (BN) has been extensively explored as an interfacial layer in SiC_f/SiC composites due to its unique multilayer lamellar structure, providing a balanced combination of moderate interfacial bonding strength, excellent oxidation resistance, and a high oxidation onset temperature (800 ºC). Moreover, when the temperature is at 950 ºC, BN can be oxidized to B_2O_3, turning to a condensed protective layer between SiC_f and SiC_m, which inhibits oxygen migration and diffusion in the SiC_f, thus maintaining passivation[11]. Kazuya et al. crafted SiC/SiC composites with varying volume percentages of BN nanoparticles through the spark plasma sintering (SPS) method. These composites demonstrated a quasi-tough fracture response, characterized by a brief nonlinear region and considerably shorter fiber pullouts owing to the relatively high modulus[12]. Moreover, enhancing the damage resistance of the SiC matrix stands as a significant challenge in the ongoing effort to further enhance the toughness

of SiC_f/SiC composites. The limited damage resistance of the SiC matrix leads to relatively low threshold stress and strain levels, rendering it susceptible to premature matrix damage under stress. To bolster the durability of SiC_f/SiC composites, one viable approach is the incorporation of nano-scale reinforcements with exceptional mechanical properties into the matrix. This strategy can disrupt or branch the propagation of primary cracks within the matrix. A prominent example of such materials is carbon nanotubes (CNTs) [13, 14]. CNTs offer numerous advantages, including their lightweight nature, high aspect ratio, stability in chemical properties, and outstanding mechanical characteristics[15]. In-situ growth of CNTs on the fibers by chemical vapor deposition (CVD) is an efficient method to prepare the CNTs/fiber-reinforced composites with controllable length and growth density[16, 17, 18]. Zhao et al. prepared SiC_f/SiC composites by PIP process by growing CNTs in situ on SiC fabrics via a thermal CVD process. The results indicated that CNTs had no significant effect on the density, porosity, and thermal conductivity of SiC_f/SiC composites, but the mechanical properties were significantly improved due to the weak bonding interphase[19]. Sun et al. prepared CNTs reinforced SiC_f/SiC composites by in situ growth of CNTs on SiC via a CVD process. The secondary pull-out of CNTs from the matrix consumes the deformation energy and thus improves the mechanical properties of CNTs-SiC_f/SiC composites[20]. Zhen et al. prepared SiC_f/SiC composites by introducing vertically aligned CNTs in situ onto PyC interface via a CVD process. In comparison to SiC_f/SiC composites featuring PyC interfaces, the introduction of PyC-VACNTs interfaces into SiC_f/SiC composites resulted in a notable increase in both flexural strength and fracture toughness. This enhancement in the mechanical properties of SiC_f/SiC composites is attributed to the modification of PyC interfaces with VACNTs, which promotes various mechanisms such as increased fiber pull-out, enhanced interfacial debonding, crack branching, and deflection[21].

A detailed examination of the structure is of paramount importance for gaining a comprehensive understanding of the structure-property relationships within composites, particularly with regard to the interfacial region. Extensive efforts and endeavors have been dedicated to unraveling the intricacies of the interface, aiming to optimize the potential

performance of fiber-reinforced composites[22, 23, 24]. However, due to the nano- or microscale thickness of the interface, an in-depth understanding of the interface is quite difficult. To overcome the above-mentioned limitations, high-resolution transmission electron microscopy (HR-TEM) in combination with energy dispersive spectroscopy (EDS) has been intensively applied in recent years. Wu et al. have successfully identified the interphase region between a carbon fiber and epoxy using HR-TEM[25]. Yang et al. have investigated the MAX phase in the SiC_f/SiC composites by HR-TEM. The results showed that two Ti_3SiC_2 layers form the whole film, where the Ti_3SiC_2 grains have different features[26].

In this work, BN and CNTs were Progressively coated on the SiC_f by CVD method to form a hierarchical structure. The SiC_f/SiC composites were fabricated by PIP methods. To investigate the enhancement of interface by each part, three composites SiC_f-CNTs/SiC, SiC_f@BN/SiC, and SiC_f@BN-CNTs/SiC were prepared. The components and microstructures of the three composites were carefully characterized by high-resolution electron transmission microscopy, X-ray analysis techniques, Raman spectroscopy, etc. The tensile strength and toughness of the three composites were tested and compared by uniaxial tensile tests.

2 Experiments and characterizations

2.1 Materials

The substrate used in this work was a third-generation SiC fiber (SiC_f) bundle (Cansas-3303, supplied by Fujian Liya New Material Co, Ltd). Boron Nitride coated SiC_f (SiC_f@BN) was provided by the Beijing Institute of Aerospace Materials, CAF. BN coatings were deposited on SiC_f by CVD with NH_3, H_2, BCl_3, and Ar as gaseous precursors as shown in Fig.1[27]. Other chemicals used were listed in Table S1 (Supplementary material).

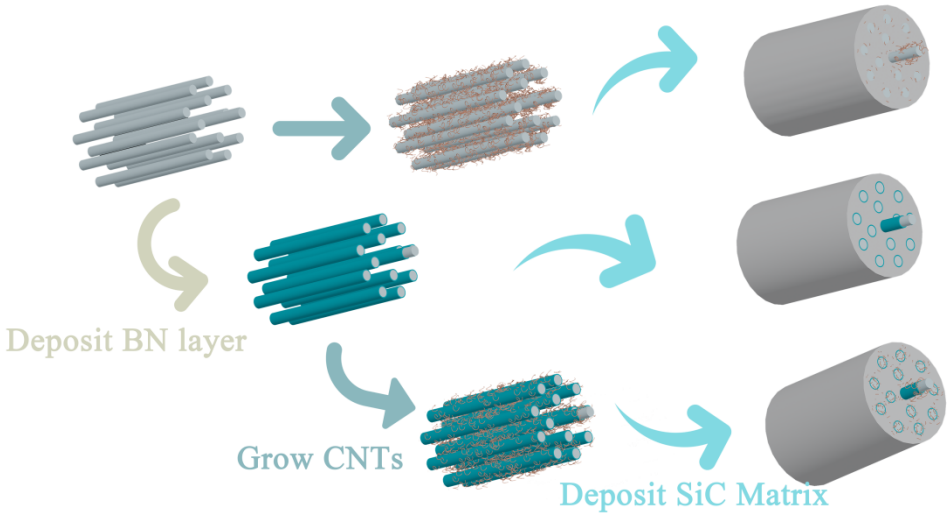

Fig.1 Schematic diagram of the fabrication procedures for SiC_f-CNTs/SiC, SiC_f@BN/SiC, and SiC_f@BN-CNTs/SiC composites.

2.2 In situ growth of CNTs

SiC_f was subjected to air desizing at 600°C for a duration of 120 minutes. Then, the processed SiC_f was immersed in 0.02 g/ml ferrocene/xylene solution for 24 h. With H_2 and Ar as the carrier and protective gas, C_2H_2 as the carbon source, and 0.05 g/ml of ferrocene/xylene solution as the catalyst precursor, the reaction was carried out by CVD at 700 ℃ for 10 min to grow CNTs on the surface of SiC_f corresponding to the sample SiC_f-CNTs.

Similarly, SiC_f@BN was pre-impregnated in 0.02 g/ml ferrocene/xylene solution for 24 h. SiC_f@BN was loaded into a CVD furnace and reacted with 0.05 g/ml ferrocene/xylene solution as a catalyst precursor in an Ar-H_2-C_2H_2 atmosphere system with a flow rate ratio of 40:9:1 at 750 ℃ for 20 min. The sample of SiC_f@BN with the growth of CNTs was noted as SiCf@BN-CNTs.

2.3 Fabrication of composites

The SiC matrix composites with SiC_f-CNTs, SiC_f@BN, and SiC_f@BN-CNTs were prepared by PIP. SiC_f/SiC composites were not prepared due to the fracture of the desized SiC_f with a

brittle property when SiC_f was deposited using the PIP process as shown in Fig.S4 (Supplementary material). The PIP process was presented as follows: the modified SiC_f samples were impregnated in polycarbosilane (PCS, KH-VHPCS-1, supplied by the Institute of Chemistry, Chinese Academy of Sciences) in a vacuum for 24 h. The samples with PCS were cross-linked and cured in the tube furnace (GSL-1800x, Hefei Kejing Material Technology Co, Ltd) and pyrolyzed at 1100 ºC for 1 h to generate the SiC matrix deposited on the surface of the samples.

2.4 Sample preparation for TEM.

The three prepared composites SiC_f-CNTs/SiC, SiC_f@BN/SiC, and SiC_f@BN-CNTs/SiC were embedded into the epoxy resin by cold mounting method. The samples were prepared as metallographic specimens by grinding and polishing and then performed by focused ion beam technique (FIB) through a double-beam electron microscope (Helios 5UC) with the protection of the Pt deposited layer. In the microstructure analysis part, in order to distinguish SiC fiber and SiC matrix, the nomenclature was as follows: SiC_f was SiC fiber, while SiC_m was SiC matrix.

2.5 Characterization

Scanning electron microscopy (SEM, TESCAN MIRA3 LMU) and transmission electron microscopy (TEM; Talos, F200) as well as energy dispersive spectroscopy systems (EDS) were used to observe the morphology, microstructure, and their composition of the samples. X-ray diffraction (XRD, EMPYREAN, Netherlands) was employed to obtain the crystalline structures with the acquisition from 10º to 80º at 2º/min. Raman spectroscopy (WITec alpha300R, Germany, 532 nm laser) was used to analyze the sample's structural and compositional information. X-ray photoelectron spectroscopy (XPS, SHIMADZU AXIS SUPRA+) was employed to analyze the surface chemical composition of the samples, correcting for the binding energy of the sample charge by referencing the C 1s peak at 284.6 eV and subtracting the background using Shirley's method. Thermogravimetric analysis

(TGA, Netzsch STA 449 F3, Germany) was used to analyze the content of generated CNTs in an oxygen atmosphere from 30 ºC to 1000 ºC at a heating rate of 10 ºC/min. The magnetic properties of CNTs powder exfoliated from glass plates were investigated by a vibrating sample magnetometer (VSM, LakeShore USA 7404). The average tensile fracture strength and ultimate tensile strain of each composite were obtained by the uniaxial tensile tests conducted by a servo tensile testing machine (WBE9010B).

3 Results and discussion

3.1 Characterization of in-situ grown CNTs

3.1.1 Growth of CNTs on the SiC_f

The as-received SiC_f was polymer-derived fiber with little oxidation. As shown in Fig.2(a), the diameters of the SiC_f ranged from 12 μm to 19 μm. The chemical composition was marginally enriched with carbon. Fig.3 (a-c) showed SEM images of SiC_f-CNTs. As shown in Fig.3 (c), CNTs grew uniformly on the SiC_f with high growth density and short length. The average diameter of the CNTs is about 24 nm. Few agglomerates of CNTs and pyrolytic carbon were found on the fiber surface.

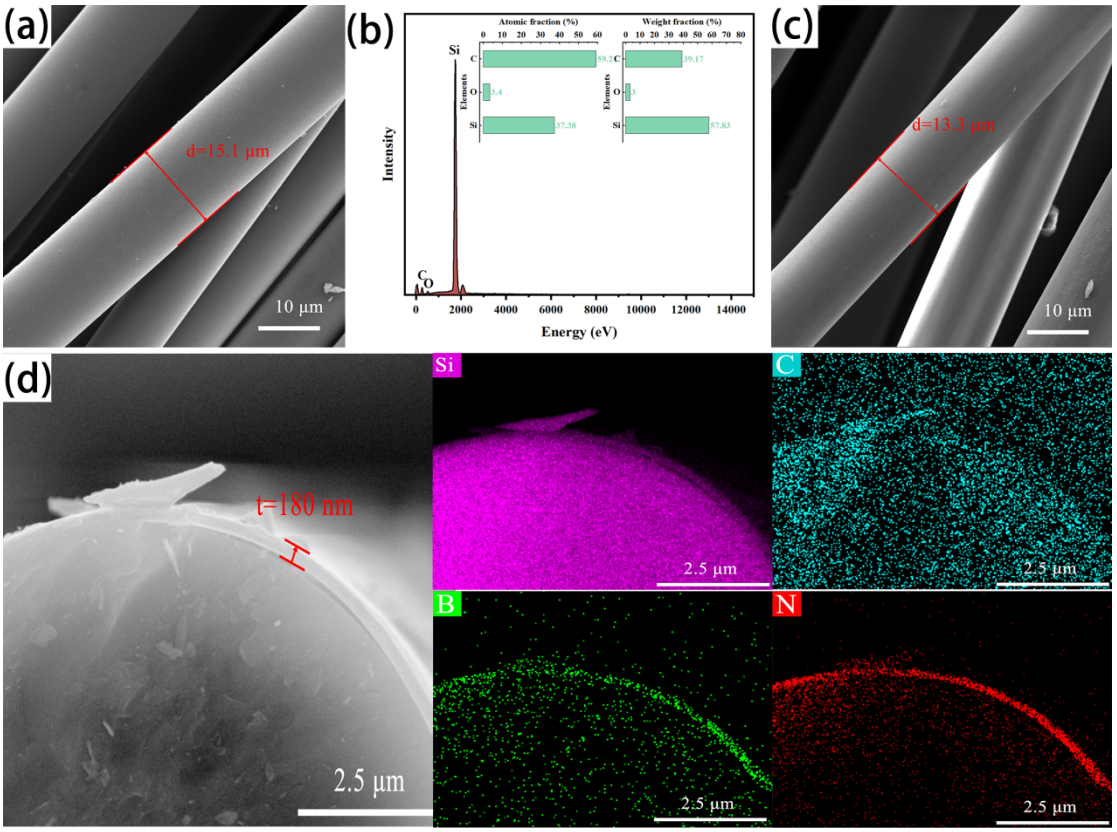

Fig.2 Characterizations of the as-received SiC_f and SiC_f@BN; (a) SEM image of SiC_f; (b) EDS analysis of SiC_f; (c) SEM image of SiC_f@BN; (d) EDS of SiC_f@BN

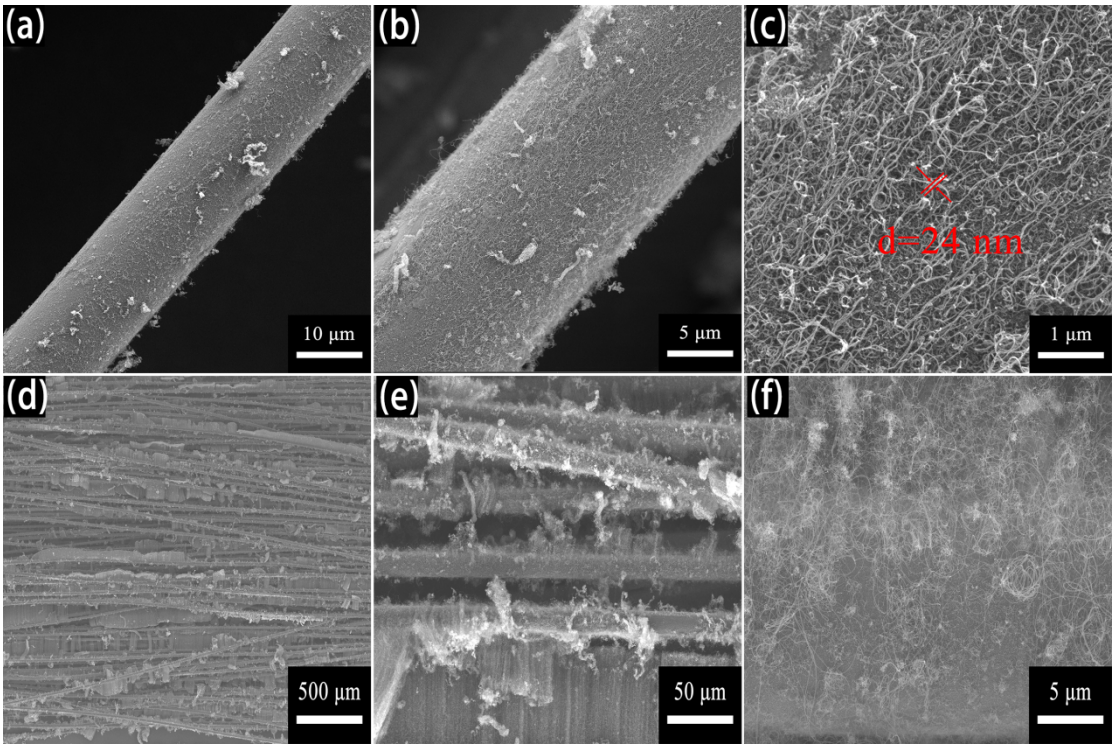

Fig.3 SEM images of SiC_f-CNTs (a-c) and SiC_f@BN-CNTs (d-f).

3.1.2 Growth of CNTs on the SiC_f@BN

Fig.2 showed that the diameters of SiC_f@BN were in the range of 12-14 μm, where the average thickness of BN coating was about 180 nm, and the elements N and B were concentrated surrounding SiC_f. As shown in Fig.3 (d), CNTs were successfully grown on the SiC_f@BN by CVD. Some CNTs wrapped on the fiber surface, and the other CNTs showed an array-like morphology with a length distribution from 40 μm to 100 μm. The diameter distribution of the grown CNTs ranged from 20 nm to 60 nm. Compared with the CNTs grown on the SiC_f surface, the CNTs grown on SiC_f@BN were less uniformly distributed and had larger diameters. There existed more pyrolytic carbon (PyC) and agglomeration of CNTs.

XRD was used to characterize the crystalline structures of the samples as indicated in Fig.4(a). All hybrids had three obvious peaks at 2θ of 35.7°, 60.1°, and 71.8°, respectively, which corresponded to (1 1 1), (2 2 0), and (3 1 1) planes of β-SiC (ICSD No. 73-1708). There was no peak of the BN phase in the XRD pattern of SiC_f@BN, which was due to the low content and poor crystallinity of the BN phase. For SiC_f@BN-CNTs, a broad diffraction peak at about 26.0° was attributed to the (002) plane of CNTs (ICSD No. 75-1621), demonstrating that the CNTs were successfully grown on the surface of SiC_f@BN by CVD.

Fig.4(b) showed TGA results of CNTs grown on the SiC_f@BN. TGA tests were conducted under an oxygen atmosphere from room temperature to 1000 ºC. There was no significant mass change of SiC_f in this temperature range. The combustion temperature of CNTs was generally in the range of 550-750 ºC[28]. As shown in Fig.4(b), at 784 ºC, the mass fraction of SiC_f@BN-CNTs decreased to 91.0%, as a maximum weight loss. Thus, the content of CNTs in SiC_f@BN-CNTs was roughly 5.5%. From 783 ºC to 993 ºC, the mass fraction of SiC_f@BN increased by 0.1%, and from 784 ºC to 993 ºC, the mass fraction of SiC_f@BN-CNTs increased by 1.7%. This could be explained by the fact that the oxidation of BN deposited on the SiC_f in the temperature range from 800 ºC to 950 ºC, B_2O_3 would be formed and then the mass of the samples was increased.

Fig.4 (c-e) exhibited the Raman results of SiC_f, SiC_f@BN, and SiC_f@BN-CNTs in 800-2000 cm^{-1}. As illustrated in Fig.4(c), the Raman spectrum of SiC_f presented two sharp peaks at 1354 cm^{-1} and 1595 cm^{-1}, corresponding to the D and G bands of the carbon materials. The two Raman bands for D-band and G-band were derived from the Raman-active in-plane atomic displacement E_{2g} mode and disorder-induced features respectively, attributed to finite particle size effect or lattice distortion[29]. These peaks originated from the carbon packets in the fibers, and the two sharp peaks represented well-bound carbon in carbon packets[30]. The intensity ratio of the D band to the G band (I_D/I_G) was generally applied to quantify the degree of graphitic ordering of carbon materials. whereby, the value of I_D/I_G for SiC_f was 1.56. The SiC_f peaks could not be detected due to their strong optical absorption and the Raman scattering efficiency of the carbon species could be regarded as at least ten times higher than that of pure SiC[31]. From the Raman spectrum of Fig.4 (d), it could be observed that there was a broad peak located near 1316 cm^{-1}, which was the E_{2g} band generated by the B-N bond vibrations and corresponded to the characteristics of h-BN[32]. The width and intensity of the peak indicated the low crystallinity of the deposited BN interfacial phase. The information on the crystallinity of CNTs in SiC_f@BN-CNTs was obtained by Raman spectroscopy (Fig.4 (e)). The value of I_D/I_G decreased to 0.97 for SiC_f@BN-CNTs compared to that of SiC_f, indicating that the long-range ordered crystalline perfection of the sample increased due to the growth of CNTs.

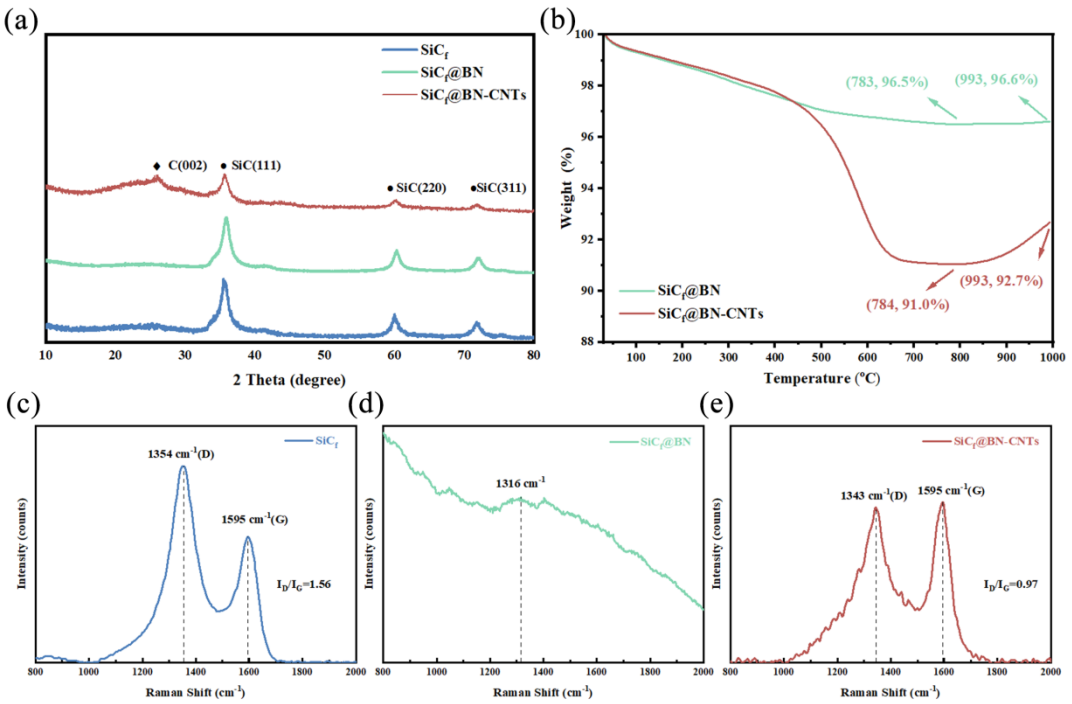

Fig.4 (a), XRD patterns of SiC_f, SiC_f@BN, and SiC_f@BN-CNTs ; (b), TGA of SiC_f@BN and SiC_f@BN-CNTs; (c-e), Raman spectra for samples in 800-2000 cm^{-1}.

Fig.5 showed the XPS patterns of the samples, and the binding energies of different bonds were listed in Table S2. The deconvoluted XPS patterns of the C 1s and Si 2p electronic states of SiC_f were shown in Fig.5(a),(b). The C 1s peak could be decomposed into C-Si, C=C, C-C, and C-O peaks and the Si 2p peaks could be decomposed into Si-C, O-Si-C, and Si-O peaks[33, 34, 35]. The Si-C bond attributed to the SiC compound appeared at 101.0 eV. The Si-O bond in the SiO_2 compound had a binding energy of 104.0 eV. The three lower components at 101.6, 102.2, and 102.6 eV were identified as O-Si-C bonds in the Si-O_xC_y (x+y = 4) compound[33]. The above analysis indicated the presence of Si-O_xC_y (x+y = 4) amorphous phase, SiO_2 phase, and carbon-rich carbon package on the SiC_f. The wide scan XPS spectrum of SiC_f@BN was illustrated in Fig.5(c). The results inferred that the content of Si in SiC_f@BN was very small (about 2.07%), indicating that the deposited BN coating was well encapsulated. The B 1s peak could be decomposed into B-N and B-O peaks, indicating the existence of B_2O_3[36]. The wide scan XPS spectrum of SiC_f@BN-CNTs was shown in Fig.5(e). Compared to SiC_f@BN, the content of C in SiC_f@BN-CNTs increased from 33.98% to 90.54%, indicating a large

amount of CNTs growth in the sample. By fitting the curves by the Voigt function, the C 1s spectrum of SiC_f@BN-CNTs could decompose into two bands of C=C and C-C. The binding energy of the C atoms bound to the defects by dangling bonds was greater relative to the graphitic C atoms. Thus, the dominant C=C band belonged to the C atom bound to the graphite network, and the weaker C-C band was attributed to the C atom at the defects[29]. The content of the C=C band was 77.83%, much more than the 22.17% of the C-C band, indicating a high crystallinity of the grown CNTs.

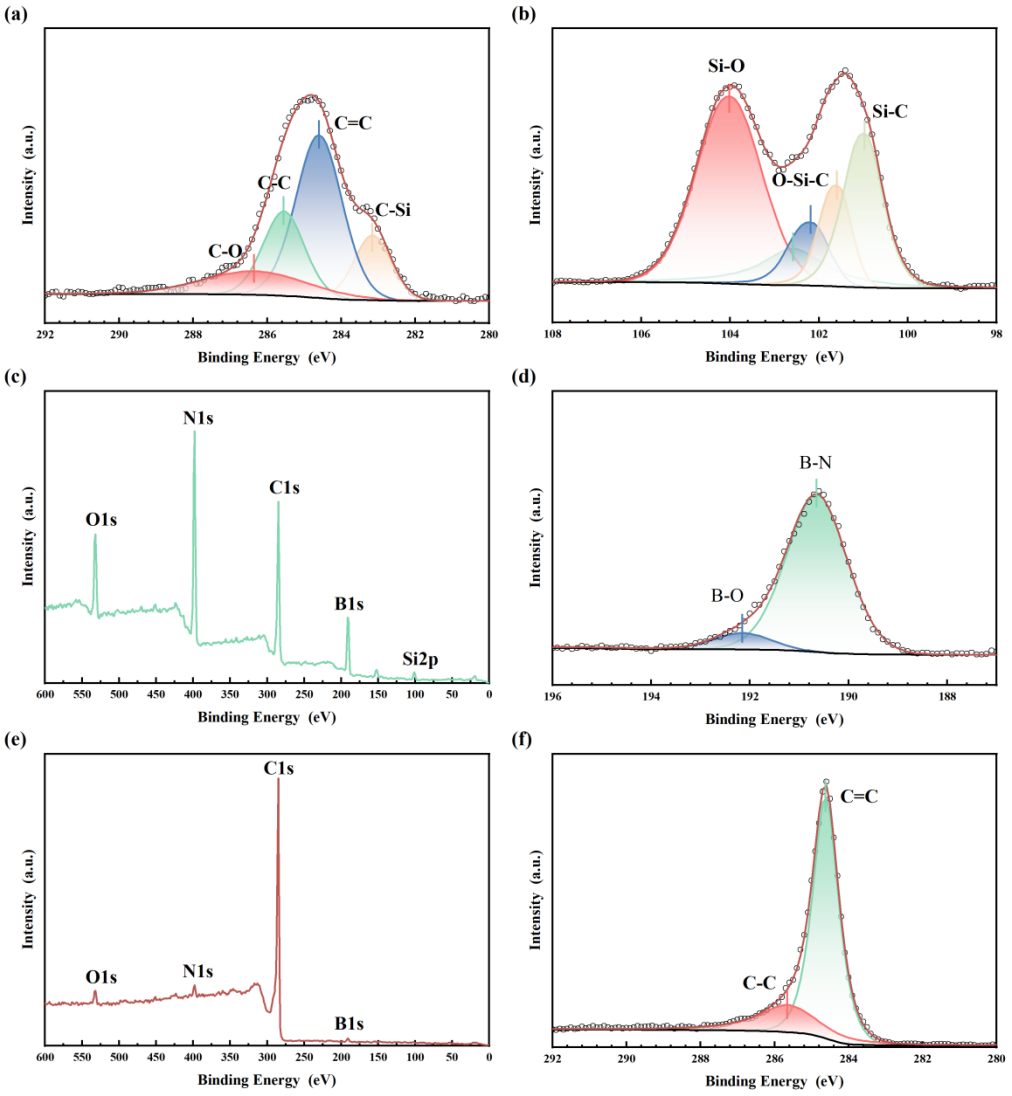

Fig.5 XPS patterns for samples; XPS C 1s (a) and Si 2p (b) spectrum of SiC_f; wide scan XPS pattern (c) and B 1s spectrum (d) of SiC_f@BN; Wide scan XPS pattern (e) and C1s spectrum (f) of SiC_f@BN-CNTs.

3.2 Interfacial characterization of composites

3.2.1 SiC_f –CNTs/SiC

As shown in Fig.6(a), the thin foil of SiC-CNTs/SiC for TEM observation was prepared with FIB. The interface of SiC-CNTs/SiC with a thickness of 798 nm was thinned more rapidly by the FIB process compared to the fibers and matrix, indicating a softer interface under ion irradiation. Fig.6(e-f) exhibited high-resolution transmission electron microscopy (HRTEM) images of the interface and matrix binding region. CNTs were grown in the interface with a thickness of about 300 nm. The metal catalyst particle size was about 20 nm, while the diameter of CNTs was in the range of 6-8 nm. Fig.6(d) showed the HRTEM and selected area electron diffraction (SAED) images of the SiC_f with the presence of continuous concentric rings, which had obvious geometrical characteristics of polycrystalline electron diffraction patterns. By calculating the radius of the continuous concentric circles, the crystallographic spacing of each grain could be obtained, and by comparing the PDF card, the SAED pattern of SiC_f could be calibrated, which showed the (111), (220), and (311) crystallographic planes of the β-SiC crystal, indicating the existence of different crystal orientations of SiC_f. The (111) crystallographic plane has the largest diffraction ring intensity. The HRTEM of the SiC_f also showed distinct stripes with different orientations, and the grain plane spacing was 0.249 nm as measured for the (111) grain plane of the β-SiC crystal. Fig.6 (h) showed the HRTEM and SAED images of the interface. The ring-like diffuse scattering halo in the SAED pattern, and the absence of distinct stripes in the HRTEM image, indicated its amorphous structure. As shown in Figure 7(i), CNTs were grown along the surface of the metal catalyst particles. The SAED diagram of the metal particles (inset in Fig 7(i)) exhibited concentric rings indicating a polycrystalline structure. By calculating the spacing of each crystalline plane and comparing the PDF cards, the metal particles were Fe_3C phase (ICSD No. 89-0951). The three diffraction rings in the diffraction pattern (inset in Fig.6(i)) were corresponding to Fe_3C <200>, <311>, and <042> reflections. The crystal plane spacing of 0.258 nm for Fe_3C crystals in the red region was attributed to the (200) crystal plane. During the growth of CNTs on the surface of SiC_f, the array-like CNTs were grown on the glass plate holding SiC_f meanwhile as shown in

Fig.S5. To further demonstrate the phase of the CNTs-coated Fe particles, the CNTs powders exfoliated from the glass plates were characterized by XRD and VSM. The XRD patterns (Fig.S6) indicated the presence of the Fe_3C phase (ICSD No. 89-2867) and α-Fe (ICSD No. 87-0721) phase in the CNTs powders. The magnetic properties were investigated with VSM at room temperature as shown in Fig.S7. The saturation magnetization intensity of CNTs powder was 18.4 emu/g, which was comparable to those reported in the literature for large-size Fe_3C-filled CNTs[37]. Thus the CNTs-coated Fe particles were the in situ released α-Fe phase and the Fe_3C phase generated by the reduced reaction rate and catalyst poisoning[38]. The non-periodic heterogeneous distribution in the HRTEM image of SiC_m indicated its amorphous structure, whose SAED pattern displayed a broader halo.

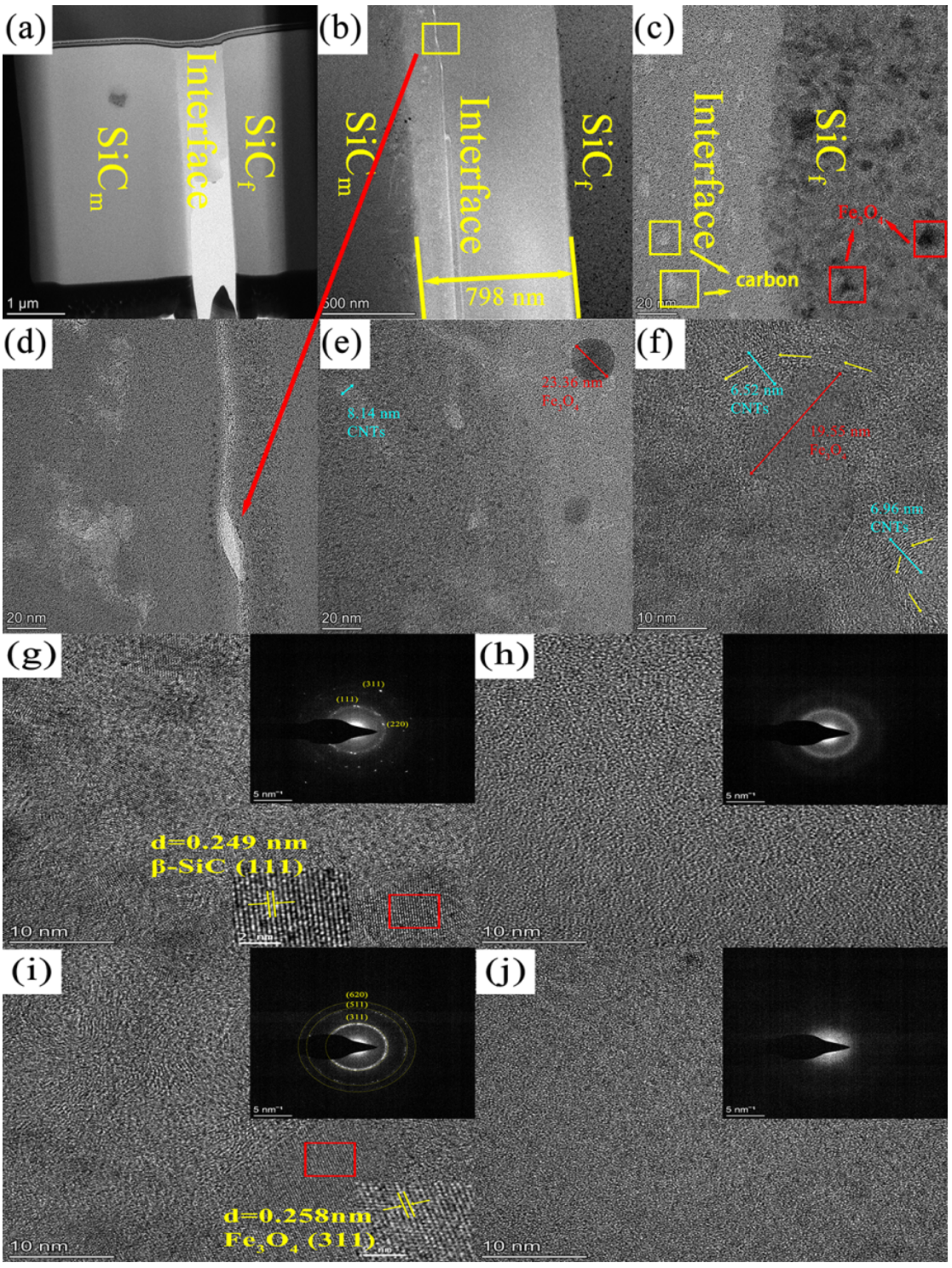

Fig.6 TEM images of SiC_f-CNTs/SiC composites, low magnification morphology, (a-b); HRTEM images of SiC_f bound region with the interface (c), the interface (d), the interface bound region with SiC_m (e) and the SiC_m (f); HRTEM and SAED images of SiC_f@BN/SiC composites, (g): SiC_f; (h): the interface; (i): the Fe particle; (j): SiC_m.

The EDS spectra of SiC_f-CNTs/SiC were employed to analyze the elemental distribution of the samples and to determine the composition of the different regions as shown in Fig.7. The stoichiometric ratio of element C, Si for SiC_f was 0.73, while the element O content was rarely 3.3%. It was notable that the presence of 0.6% Fe in area #1 suggested the diffusion of Fe particles into the interior of SiC_f. The dark specks appeared in the BF-TEM (Fig.6 (c)) reflecting the distribution of Fe particles in the fibers. In addition, widespread bright specks with a size of about 10 nm were present at the interface near the fibers. A comparison of the percentage of each element in Areas #2 and #3 indicated that the bright specks were the amorphous enriched carbon. As shown in Fig.7(b), the interface (Area #2, #3) had the lowest elemental carbon content and the highest elemental O content compared to the other regions; meanwhile, the elemental Si, O stoichiometry ratio was close to 1:2. Therefore, the interface was mainly made up of the SiO_2 phase. The SiC_f/SiC composites prepared by the PIP process reported by Wang et al. also had an oxide layer with a thickness of about 300 nm in the middle of the interface and the matrix, which was thought to be related to the low initial temperature of the matrix preparation[39]. The generation of this interfacial layer may be due to several reasons: firstly, SiC_f underwent a passive oxidation reaction during the desizing in air, and the SiO_2 film was formed on the surface, at the same time generating amorphous enriched carbon widely distributed in Area #2[40].

$$2SiC(s) + 3O_2(g) \rightarrow 2SiO_2(s) + 2CO(g) \quad (1)$$

$$SiC(s) + 2O_2(g) \rightarrow SiO_2(s) + CO_2(g) \quad (2)$$

Secondly, during the preparation of CNTs and the matrix, due to the lack of interfacial protection, SiC_f was oxidized and corroded, generating the SiO_2 phase. A bright line was present at the interface near the matrix as shown in Fig.6(b), and (d) showed an enlarged view of the yellow rectangular area in Fig.6(b). In Fig.7(a), the mapping of elements in the bright line region was highlighted by the yellow rectangle. The bright line was pyrolytic carbon (PyC), which was formed by C_2H_2 pyrolysis during the growth of CNTs by CVD. The CNTs grew along the curved perimeter of the Fe particles, concentrating mainly on the bonding areas of the interface and the matrix. The catalyst Fe particles were less uniformly distributed,

and some agglomerates formed larger size particles. The size of Fe particles was in the range of 3-25 nm. The growing CNTs were uniformly distributed along the horizontal direction of the interface. However, the diameter and length of CNTs were distributed in a wide range. The diameter of CNTs was in the range of 5-15 nm, which was proportional to the size of Fe particles and the length of CNTs was in the range of 50-150 nm[41]. Area #6 corresponded to the area of SiC_m with higher oxygen content (11.9 at%), which was attributed to the generated SiC_xO_y amorphous phase and SiO_2 phase.

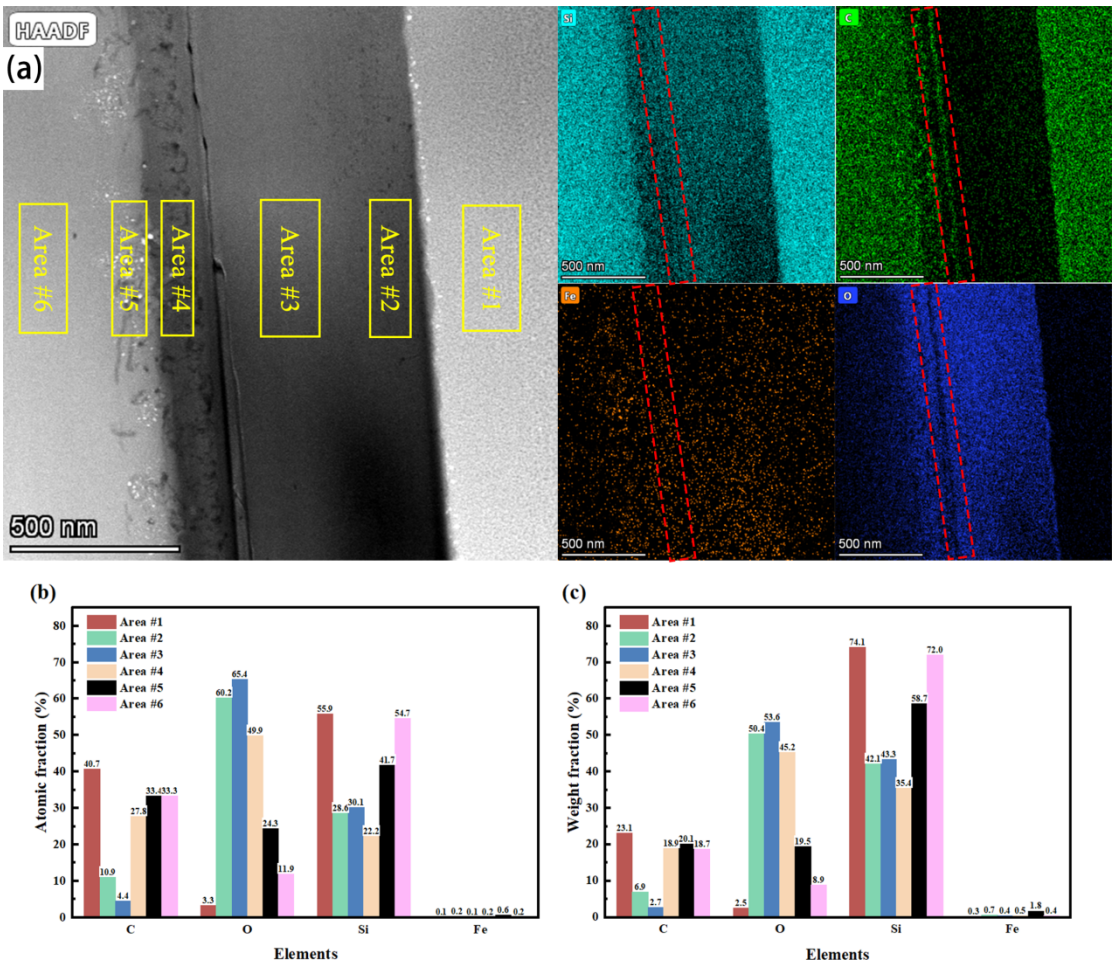

Fig.7 EDS spectrum of SiC_f-CNTs/SiC composites; the mapping of elements (a); histogram of the percentage of each element in different regions, (b) atomic fraction; (c) weight fraction.

The EDS spectrum of the area of the interface and matrix combination was shown in Fig.S8. In DF-TEM, the bright specks (Area #2) were the Fe particles, while the dark line (Area #3) was the CNTs. Some of the CNTs grew around the Fe particles and parts extended outward

from the Fe particles. The growth pattern of CNTs in this system was "bottom-growth" because of the strong interaction between Fe particles and SiO_2 as shown in Fig.S8 (a)[42].

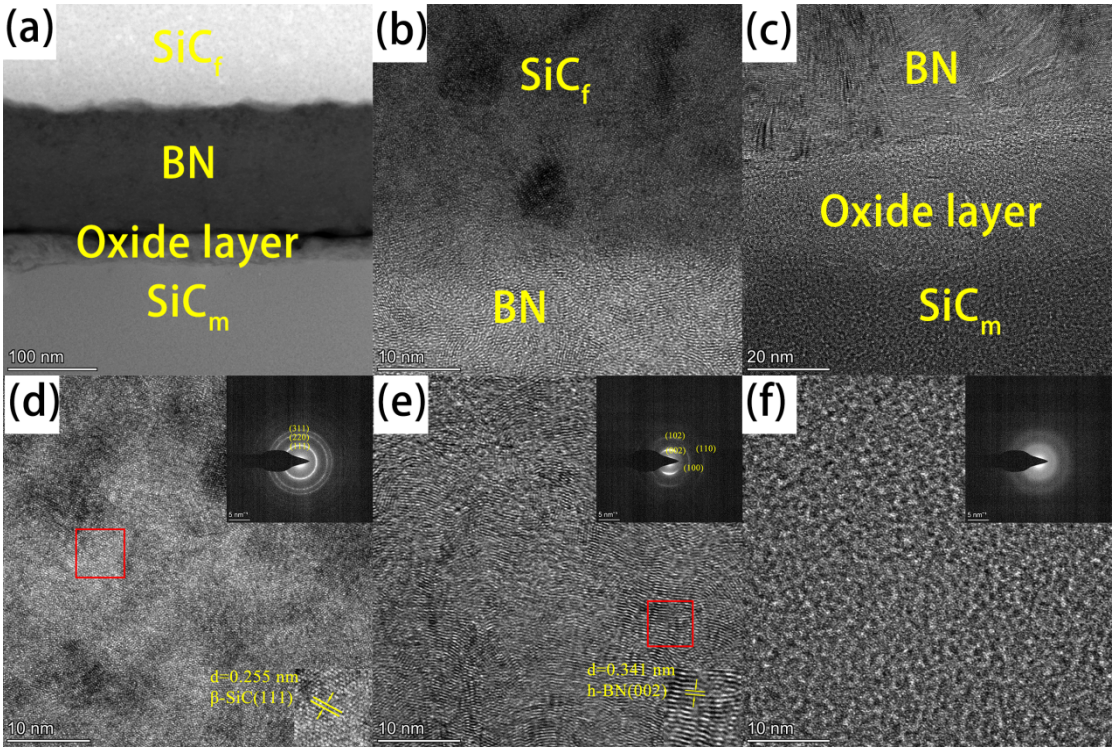

Fig.8 TEM images of SiC_f@BN/SiC composites, low magnification morphology (a); HRTEM images of SiC_f bound region with BN (b) and BN bound region with SiC_m (c); HRTEM and SAED images of SiC_f@BN/SiC composites, (d): SiC_f; (e): BN; (f): SiC_m.

3.2.2 SiC_f@BN/SiC

As shown in Fig.8, the microstructure of SiC_f@BN/SiC composites was characterized by TEM. Fig.8(a) showed the microscopic morphology at the interface of the composite. The BN interface connected the fiber and the matrix. The BN interface and SiC_f were well bonded, and the thickness of the BN layer was about 140 nm. There existed a transition layer with a thickness of about 30 nm between the BN and the matrix, which was indicated as an oxide layer by the EDS analysis later, and the layer had debonding with poor adhesion to the matrix. As shown in Fig10(b),(c), SiC_f had a long-range ordered crystalline structure while SiC_m had an amorphous structure. In addition, a multilayer lamellar structure similar to graphite existed at the BN interface.

Fig.8(d) showed the HRTEM and SAED images of the SiC_f with the presence of continuous concentric rings, as similar to the SiC_f in SiC_f-CNTs/SiC. The SAED pattern of SiC_f showed the (111), (220), and (311) crystallographic planes of the β-SiC crystal, indicating the existence of different crystal orientations of SiC_f. The HRTEM of the SiC_f showed the grain plane spacing was 0.255 nm, which was slightly larger than that of SiC_f in SiC_f-CNTs/SiC. Fig.8(e) exhibited the HRTEM and SAED images of the BN interface. The SAED pattern of the calibrated BN interface showed that the crystal was hexagonal BN (h-BN), and the figure displayed the (002), (100), (102), and (110) crystallographic planes of h-BN. The HRTEM image of h-BN confirmed that the crystalline plane of the crystal in this region was the (002) plane, of which the spacing was 0.341 nm. The SAED pattern was a typical turbulent layer material with overall structural anisotropy, which was also confirmed by the streaks with different orientations in HRTEM. Throughout the coating, the preferential orientation of the BN atomic layer was parallel to the fiber surface. At the interface close to the fibers, the first deposited atomic layer followed the roughness of the fibers. There was a structural continuity between the two regions, and the atomic layer of BN was locally very deformed, ensuring the connection with SiC_f[43]. Fig.8 (f) showed the HRTEM and SAED images of the SiC_m prepared by the PIP process. The SAED pattern of the SiC_m was a ring-like diffuse scattering halo revealing the amorphous structure of the matrix. The HRTEM image of SiC_m without obvious stripes also indicates its amorphous structure.

Fig.9 showed the EDS spectrum of SiC_f@BN/SiC. In Area #1, the stoichiometric ratio of element C, Si for SiC_f was close to 1:2, while the element O content was rarely 2.6%. In Area #2, which was the BN interface near the SiC_f, the atomic fraction of oxygen was 12.0%, which was higher than the oxygen content of 3.1% within the BN interface (Area #3). This was attributed to the passivation reaction of SiC_f in the air to form a SiO_2 layer. In addition, oxygen was readily absorbed to form dangling bonds on BN or substituted into the BN structure to form the BN_xO_y phase[44]. Oxygen absorption led to a reduction in the oxidation resistance of the BN interface, therefore, a low oxygen content was required to be maintained during the deposition of BN. A transition layer (Area 4) existed in the area of the combination

of the BN interface and the SiC_m, which was enriched in carbon and oxygen elements. The mapping of the elements in this region was highlighted by the red rectangle. It was worth noting that element N was discontinuously distributed in the transition layer, so the transition layer may be the interface layer was corroded and part of BN was oxidized[40].

$$4BN(s) + 3O_2(g) \rightarrow 2B_2O_3(l) + 2N_2(g) \qquad (3)$$

In DF-TEM (Fig.9(a)), between BN and the transition layer, there was a layer of enriched carbon with a multilayered structure similar to BN as indicated by the dark region. The carbon enrichment was attributed to the high carbon content of the PCS itself used in the PIP process, with a C/Si ratio close to 2. The presence of the carbon-rich layer was favorable for material toughening, but it was almost oxidized above 1000 ºC, which reduced the mechanical properties of the composites. In addition, the content of oxygen element was 28.5%, higher than that of all other areas demonstrating the presence of SiO_2. The generation of this transition layer could be attributed to the oxygen contamination produced by the FIB milling and the oxidation reaction during the SiC_m preparation. The above analysis revealed that the presence of the BN interface prevented the oxidation and corrosion of SiC_f compared to SiC_f-CNTs/SiC. The high oxygen content (17.6%) in the prepared matrix was due to the presence of the Si-C_xO_y amorphous phase and SiO_2 phase in the SiC_m.

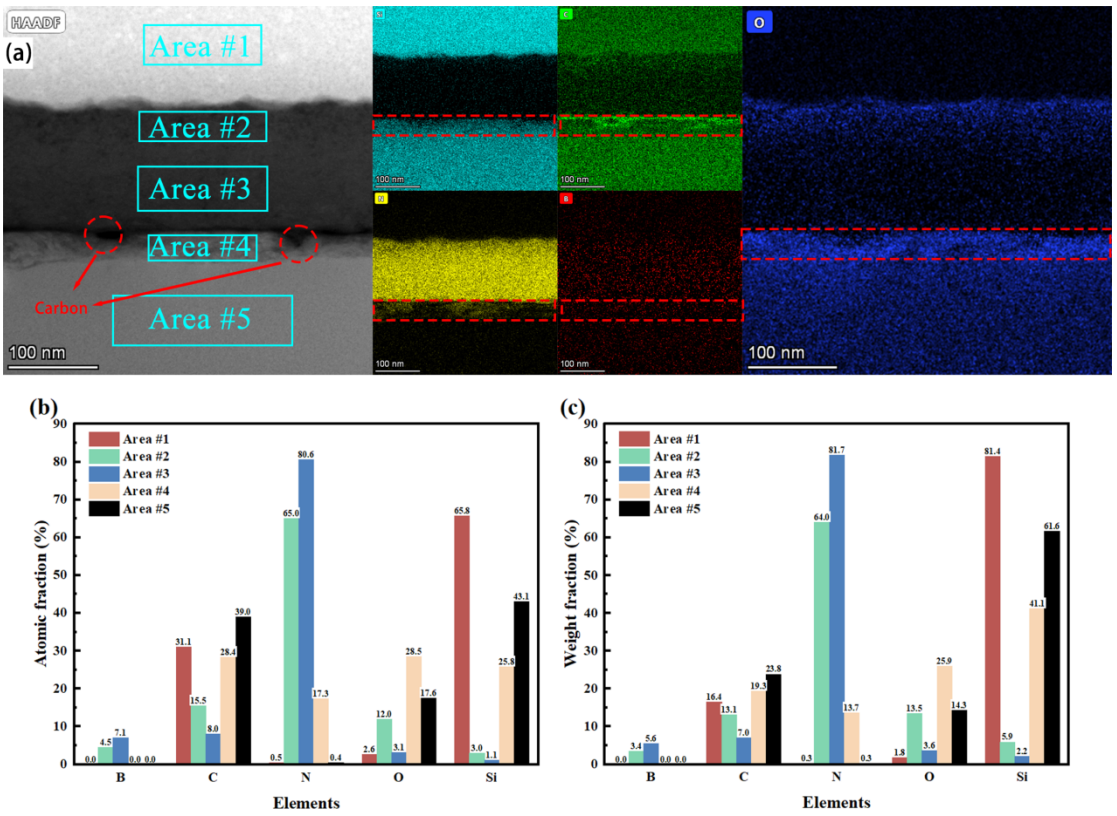

Fig.9 EDS spectrum of SiC_f@BN/SiC composites; the mapping of elements (a); histogram of the percentage of each element in different regions, (b) atomic fraction; (c) weight fraction.

3.2.3 SiC_f@BN-CNTs/SiC

As shown in Fig.10(a) and (b), the prepared SiC_f@BN-CNTs/SiC composites had a clear multilayer structure at the interface, including the BN layer, carbon enriched layer, oxide layer, and CNTs grown in the SiC_m. The size of Fe nanoparticles released in situ from ferrocene generally varied from 3 nm to 30 nm in Fig10(d). There existed a large Fe particle size up to 45.9 nm, formed by the agglomeration of small particles. Fig.10(e) and (f) illustrated the two types of CNTs growth along the Fe particles: outward extension and encapsulation growth, respectively. The diameters of CNTs were in the range of 3-6 nm, while the lengths were about 10-90 nm. Compared to SiC_f -CNTs/SiC composites, SiC_f in SiC_f@BN-CNTs/SiC composites was attributed to β-SiC, with an anisotropic polycrystalline structure. Fig.10(h) also demonstrated that h-BN was a typical turbulent layer material with anisotropy and poor crystallinity. Fig.10(i) illustrated the HRTEM image of the carbon-enriched layer, showing intermittent turbulence-like flow, and the SAED image

indicated the amorphous structure. In the SiC_f@BN-CNTs/SiC composite, the in situ released Fe particles were attributed to the Fe_3C phase with anisotropy, and the SAED pattern in this region showed the (002) crystal plane of the CNTs. As shown in Fig.10(l), the electron diffraction pattern of the selected area in SiC_m had weak concentric circles, indicating poor long-range ordering in this area. The silicon carbide matrix had an amorphous structure with some short-range/long-range ordering in some areas.

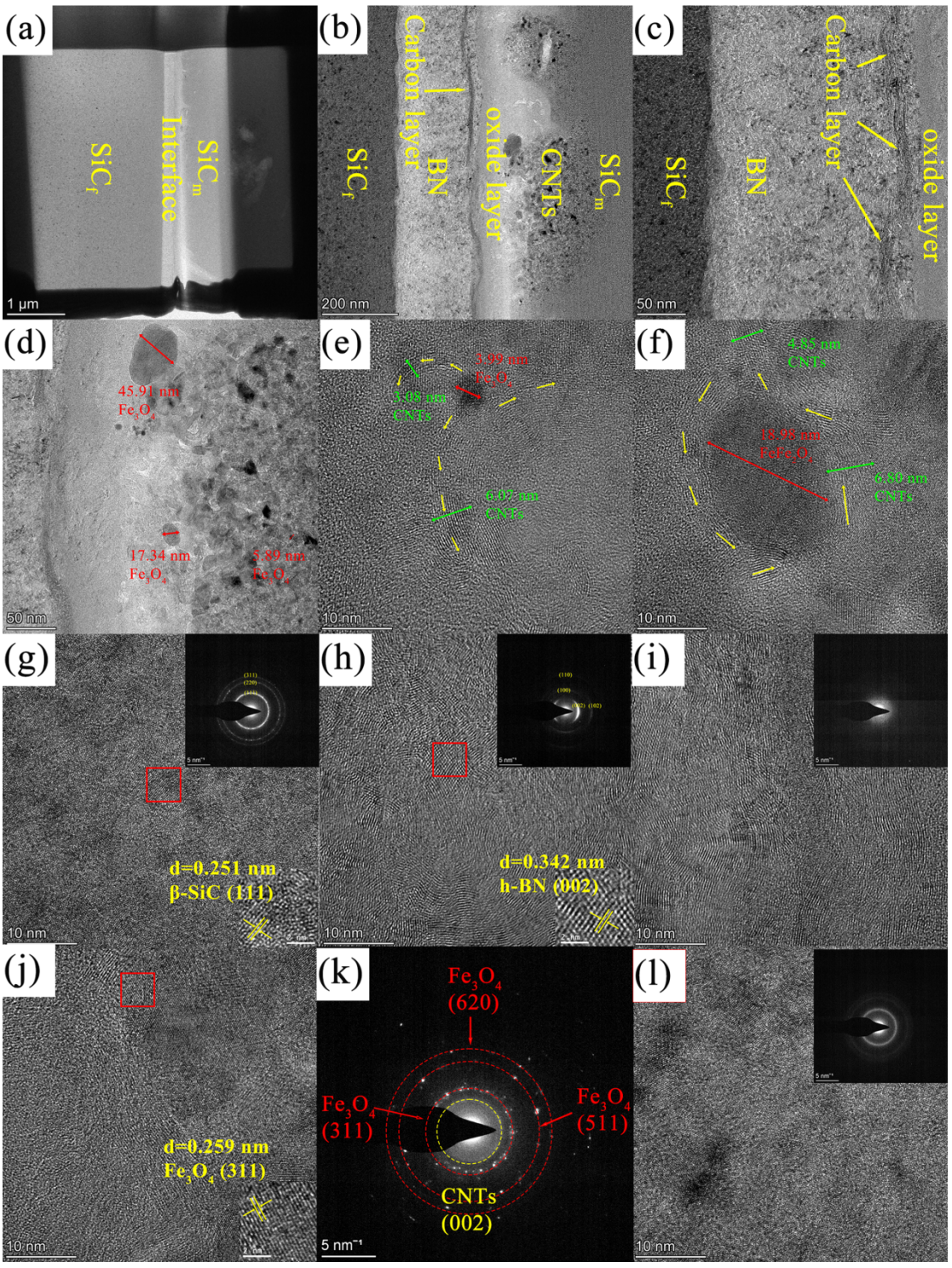

Fig.10 TEM images of SiC_f@BN-CNTs/SiC composites, low magnification morphology, (a-b); HRTEM images of SiC_f bound region with the interface (c), the interface bound region with SiC_m (d), and the SiC_m (e-f)； HRTEM and SAED images of SiC_f@BN/SiC composites, (g): SiC_f; (h): BN; (i): the enriched carbon; (j-k): Fe particles and CNTs; (l): SiC_m.

Fig.11 showed the EDS spectrum of SiC_f@BN-CNTs/SiC. The edges of the BN layer near SiC_f exhibited significant oxygen enrichment due to the presence of SiO_2 and BN_xO_y phases, similar to that in the SiC_f@BN/SiC composite. The oxygen-enriched area was marked with a blue rectangle. The BN layer with a thickness of about 220 nm was markedly corroded on the edge near the SiC_m. The corroded area (highlighted by the red rectangle) was about 10 nm in thickness and was enriched in Si, and C elements and less in O elements. The HRTEM and SAED images of this region indicated an interrupted turbulent layer and an amorphous structure. Hence PyC was found in this region along with a possible Si or SiC phase. There was a transition layer between BN and SiC_m with oxygen content up to 65.2%. This transition layer was an oxide layer with SiO_2 as the main component. It was also noted that the oxide layer was present in all three composites. Comparing the oxide layer thicknesses of the three materials: SiC_f-CNTs/SiC (798 nm) > SiC_f@BN-CNTs/SiC (90 nm) > SiC_f@BN/SiC (30 nm), and the oxygen content of the oxide layer near SiC_m: SiC_f-CNTs/SiC (65.4%) > SiC_f@BN-CNTs/SiC (65.2%) > SiC_f@BN/SiC (28.5%). It could be concluded that the oxide layer was partly generated during the growth of CNTs. Since SiO_2 was a good carrier for growing CNTs, the generation of this oxide layer promoted the growth of CNTs. After depositing the BN layer, the thickness of the oxide layer was significantly reduced, indicating that the BN layer mitigated the corrosion and oxidation of SiC_f during the growth of CNTs and preparation of SiC_m, thus ensuring the strength of SiC_f. In DF-TEM (Fig.11 (a)), according to the histogram of the percentage of each element in different regions, The bright speck in Area #3 was the Fe particle, while the dark speck in Area #4 was attributed to the CNTs. The Fe particles were less uniformly distributed with aggregation in some areas. Due to the strong bonding strength of SiO_2 and Fe particles, CNTs were grown in a “bottom growth” mode on the SiC_f@BN surface. The oxygen content in Area #6 was 8.2%, indicating that the prepared SiC_m had a low oxygen content in the part away from the interface. In SiC_m, there were carbon-enriched regions, such as the dark specks in Fig.11 (a).

Fig.S9(a) presented the enlarged area of the white rectangle in Fig.11(a). Area #2 corresponded to the BN layer, with high content of elemental O. In Fig.S9 (a), the mapping of

element N clearly showed that the BN layer was oxidized and the generated voids were occupied by elements C and Si. In addition, in the oxide layer, elements Si, and O were abundantly distributed, while the content of other elements such as C was low, indicating that the main component of the oxide layer was SiO_2.

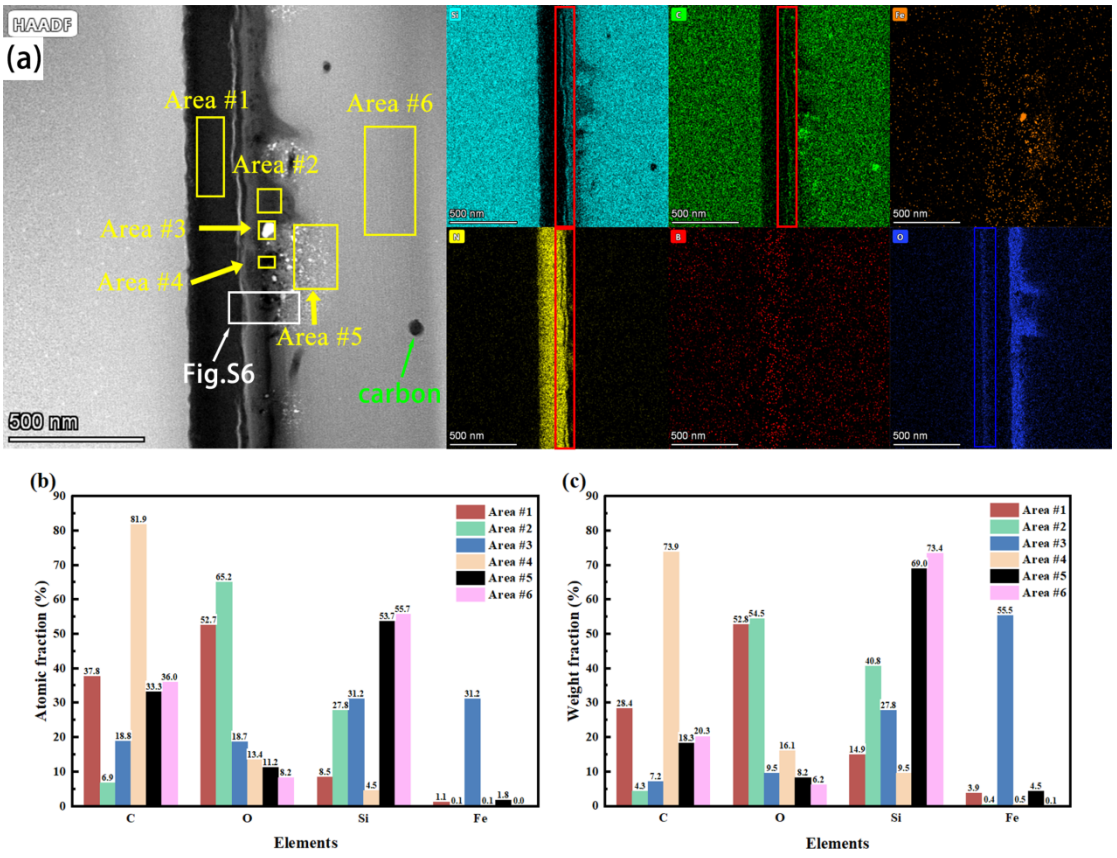

Fig.11 EDS spectrum of SiC_f@BN-CNTs/SiC composites; the mapping of elements (a); histogram of the percentage of each element in different regions, (b) atomic fraction; (c) weight fraction.

In summary, SiC_f was attributed to the β-SiC phase with a polycrystalline structure. The obtained BN had a hexagonal structure with a multilayer turbulent structure, and SiC_m had an amorphous structure with carbon enrichment in some regions. The originally released Fe catalyst particles had the polycrystalline Fe_3C phase, and Fe particle agglomerates affected the diameter of the CNTs. The growth mode of CNTs was "bottom growth", extending outward from the Fe particles or encapsulated growth. SiO_2 and BN_xO_y phases in the SiC_f and BN bonding region caused high oxygen content. In the desizing process of SiC_f, an oxide layer with SiO_2 as the main component was generated, which could promote the growth of CNTs.

The introduction of the BN layer could reduce the thickness of the oxide layer and protect the SiC_f from corrosion and oxidation. However, the outer BN layer was partially oxidized and the multilayer structure PyC phase was filled in this area.

3.3 Mechanical properties of three composites

The tensile fracture strength and ultimate tensile strain of composites with different interfaces were measured by a servo tensile testing machine as shown in Fig.12. The tensile fracture strength of SiC_f-CNTs/SiC was only 36 MPa, and the ultimate strain was only 0.6%. According to the above analysis, it was because the SiC_f was degraded by oxidation and corrosion during the growth of CNTs and deposition of SiC_m, which made the mechanical properties decrease. The BN interface in SiC_f@BN/SiC with moderate interfacial bonding strength as an interface protected the fibers from corrosion and prevented the expansion of cracks in the matrix, thus improving the mechanical properties[45]. The tensile fracture strength of SiC_f@BN/SiC was increased to 293 MPa with an ultimate tensile strain of 2.1%. The ultimate tensile strength value of SiC_f@BN/SiC composites prepared by the spark plasma sintering, as reported by Kazuya et al., was 301 ± 56 MPa[12]. This value closely resembles the tensile fracture strength of the SiC_f@BN/SiC composites discussed in this paper. BN and CNTs were used in SiC_f@BN-CNTs/SiC to synergistically reinforce the SiC_f/SiC composites. the BN layer protected the fiber from oxidation and corrosion, and the thickness of the oxide layer in the composite was decreased from 798 nm to 90 nm. the CNTs had excellent mechanical properties and were able to improve the damage resistance of the micron-scale matrix. SiC_f@BN-CNTs/SiC exhibited the largest tensile fracture strength of 359 MPa, with an improvement of 23% compared to that of SiC_f@BN/SiC. The ultimate tensile strain was 2.2%, slightly higher than that of SiC_f@BN/SiC. Thus, CNTs and BN multi-interfaces synergistically enhanced the macroscopic mechanical properties of the SiC_f/SiC composites.

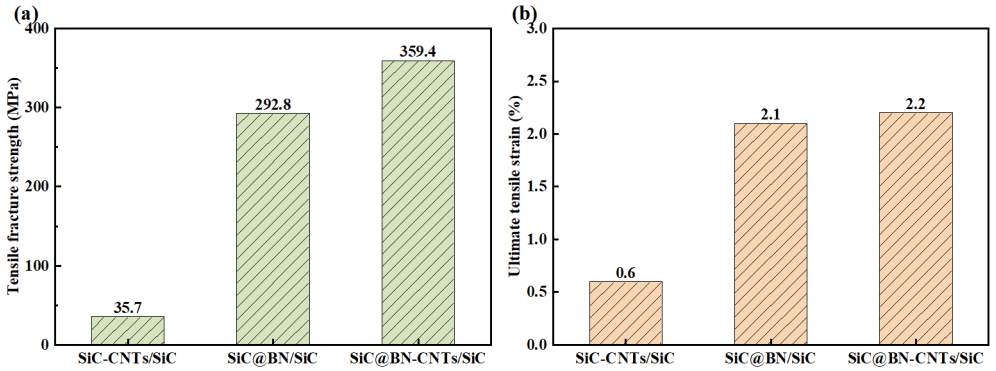

Fig.12 Mechanical properties; (a), Tensile fracture strength; (b), Ultimate tensile strain.

The fracture surfaces of SiC_f/SiC composites with different interfaces were presented in Fig.13. Both the continuous and toughened phases of SiC_f/SiC composites were brittle materials, and the main toughening mechanisms could be concluded as three points: (1) matrix crack deflection, (2) interfacial debonding, and (3) fiber pullout. For SiC_f-CNTs/SiC, the cracks in the matrix were short and formed a mesh structure by deflection (Fig.13(a)). Since the main components of the interface for SiC_f-CNTs/SiC were SiO_2 and CNTs, and SiO_2 had a considerable bond strength with SiC. When most of the cracks extended near the interface, the fibers were penetrated and showed brittle characteristics with smooth and flat fractures. Extremely few fibers were pulled out and the pull-out length was abridged, averaging only 3.9 μm. Fiber pullout could deflect the cracks that expanded along the paralleled interface direction in an edge-opened (Mode Ⅰ) crack[46]. The pull-out fibers were bonded to the matrix and there was elemental carbon enrichment in the bonding region (Fig.13(c)), indicating that SiC_f-CNTs/SiC composites exhibited a substantial interfacial bond strength. In contrast, for SiC_f@BN/SiC, the cracks extended for longer distances, primarily perpendicular to the fiber direction within the matrix without deviation. Because of the moderate strength of the BN-SiC bond, the majority of the fibers experienced interfacial debonding, resulting in more fibers being pulled out, with an average length of 27.8 μm. The presence of N elements on the surface of the pulled-out fibers (Fig.13(f)) indicated that the fibers were glued to the BN layer In addition, BN interfaces were also observed in the holes

resulting from fiber pullout. The above analysis revealed that the interface itself was debonded during fiber pullout[47]. The fracture surface of the fibers was rougher due to the deflection of the interface against the cracks. For SiC_f@BN-CNTs/SiC, the same as SiC_f -CNTs/SiC, the cracks in the matrix were deflected to form short crack networks (Fig.13(a)). The BN layer improved the bonding strength of the interfacial layer to the fibers and matrix, a significant number of interfaces were debonded and more fibers were pulled out with an average length of 16.4 μm (in SiC_f@BN-CNTs/SiC, holes resulting from fiber pull-out were more than in other composites). The pulled-out fibers had bonded BN layers on the surface (Fig.13 (k)) and also part of the interface was bonded to the matrix (Fig.13 (j)). Therefore, BN interfacial delamination and debonding occurred mainly inside the BN interface. It was also noted that some of the fibers debonding with shorter pullout occurred on the matrix, the interface and matrix contained more oxygen elements, and there were many voids in the combined region of the BN interface and matrix leading to poor load transfer and stress concentration, which accelerated the cracking and damage process of the matrix. Fig.13(l) exhibited CNTs dispersed in the matrix and there were no obvious cracks in this region.

Therefore, the introduction of CNTs could prevent and destroy cracks in the matrix to improve the damage resistance of the matrix. The SiO_2 phase produced during the growth of CNTs increases the interfacial bond strength, and by introducing the BN layer, the interfacial bond strength was improved, resulting in more fiber debonding and pull-out, which benefited the enhancements of both the tensile strength and the toughness of SiC_f/SiC composites. Enhancing the compatibility of CNTs with the matrix and reducing the generation of stress concentrations could further improve the mechanical properties of SiC_f/SiC composites.

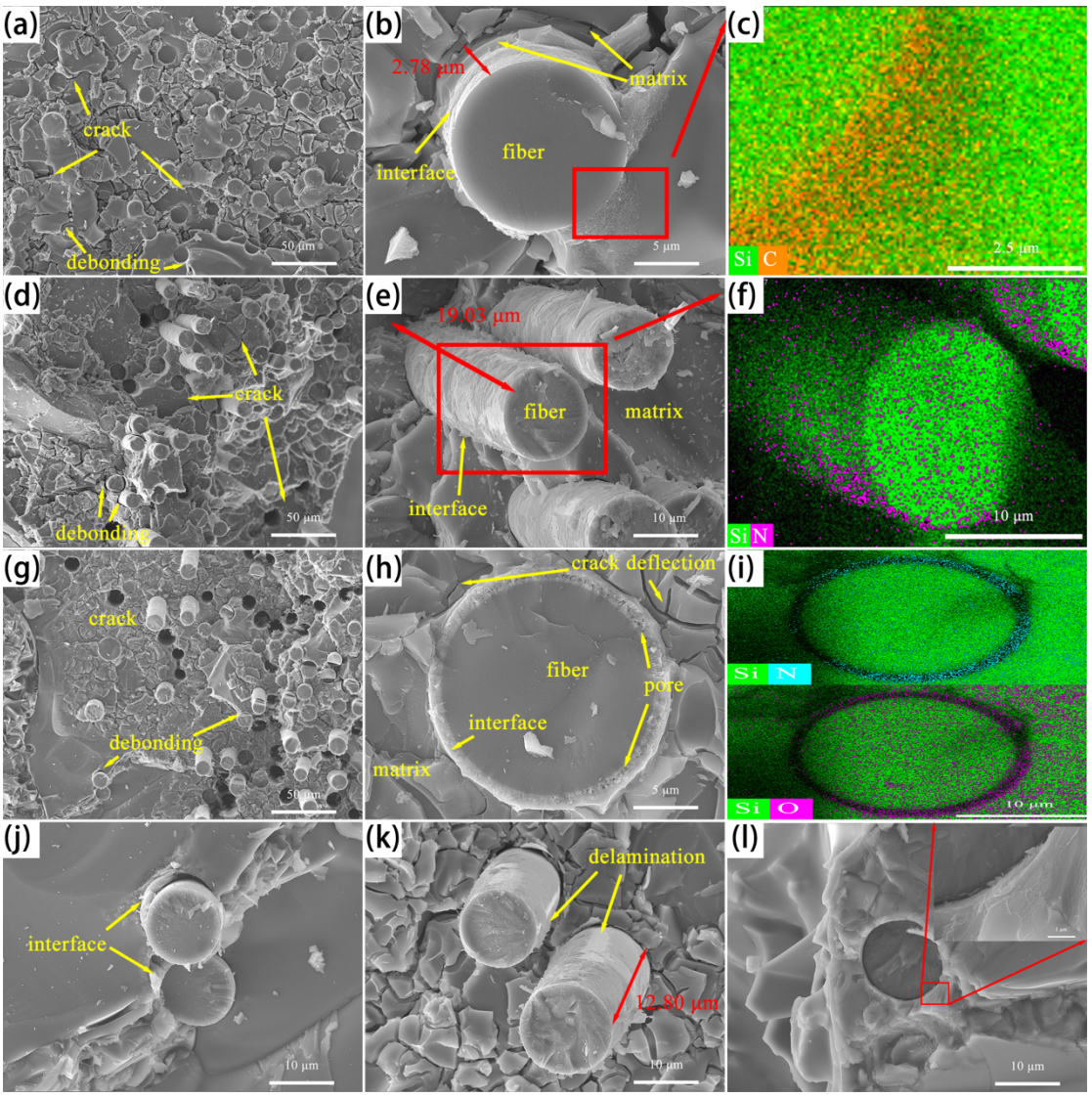

Fig.13 Fracture surface of SiC_f-CNTs/SiC (a-c), SiC_f@BN/SiC (d-f), and SiC_f@BN-CNTs/SiC (g-l).

4 Conclusion

The boron nitride (BN) and carbon nanotubes (CNTs) were progressively coated on the SiC_f by CVD method to form a hierarchical structure. The grown CNTs on the SiC_f@BN had array-like morphology with 5.5 wt% in the composite of SiC_f@BN-CNT. The SiO_2 within the oxide layer generated during the preparation process stimulated the growth of CNTs and enhanced the strength of interfacial bonding. The introduction of the BN layer reduced the thickness of the oxide layer, protected the fibers from corrosion and oxidation, and thus increased the tensile fracture strength and toughness of the SiC_f/SiC composites. CNTs could

deflect and break cracks in the matrix and improve the damage resistance of the matrix. The mechanical properties of the SiC_f/SiC composites were significantly improved by the synergistic reinforcement of CNTs and BN interfaces with a maximum tensile fracture strength of 359 MPa. The mechanical properties of the SiC_f/SiC composites could be further improved by increasing the uniformity of CNTs and improving the compatibility of CNTs with the matrix.

Declaration of Competing Interest

The authors declare that they have no known competing financial interests or personal relationships that could have appeared to influence the work reported in this paper.

Acknowledgment

This work is supported by the National Natural Science Foundation of China (Grant No. 52002403), the Natural Science Foundation of Hunan province (Grant No. 2022JJ40607), and the key project of Changsha (Grant No. kh2103011).

Data Availability Statements

The datasets generated during and/or analyzed during the current study are available from the corresponding author on reasonable request.

References

1. N. P. Padture, "Advanced structural ceramics in aerospace propulsion," *Nature Materials,* 15[8] 804-09 (2016).
2. M. Li, X. Zhou, H. Yang, S. Du, and Q. Huang, "The critical issues of SiC materials for future nuclear systems," *Scripta Materialia,* 143 149-53 (2018).
3. V. d. V. M. H and N. M. R., "CMCs: Research in Europe and the Future Potential of CMCs in Industry,″ pp. 2-21 in Proceedings of the 20th Annual Conference on Composites, Advanced Ceramics, Materials, and Structures—B: Ceramic Engineering and Science Proceedings. Vol. 17.
4. S. Yajima, J. Hayashi, and M. Omori, "CONTINUOUS SILICON CARBIDE FIBER OF HIGH TENSILE STRENGTH," *Chemistry Letters,* 4[9] 931-34 (1975).
5. T. F. Cooke, "Inorganic Fibers-A Literature Review," *Journal of the American Ceramic Society,* 74[12] 2959-78 (1991).
6. N. Carrère, E. Martin, and J. Lamon, "The influence of the interphase and associated interfaces on the deflection of matrix cracks in ceramic matrix composites," *Composites Part A: Applied Science and Manufacturing,* 31[11] 1179-90 (2000).
7. H. J. Yu, X. G. Zhou, W. Zhang, H. X. Peng, C. R. Zhang, and Z. L. Huang, "Mechanical properties of 3D KD-I SiCf/SiC composites with engineered fibre–matrix interfaces," *Composites Science and Technology,* 71[5] 699-704 (2011).
8. T. Nozawa, T. Hinoki, A. Hasegawa, A. Kohyama, Y. Katoh, L. L. Snead, C. H. Henager, and J. B. J. Hegeman, "Recent advances and issues in development of silicon carbide composites for fusion applications," *Journal of Nuclear Materials,* 386 622-27 (2009).
9. H. Liu, L. Li, J. Yang, Y. Zhou, Y. Ai, Z. Qi, Y. Gao, and J. Jiao, "Characterization and modeling damage and fracture of prepreg-MI SiC/SiC composites under tensile loading at room temperature," *Applied Composite Materials,* 29[3] 1167-93 (2022).
10. R. R. Naslain, R. J. F. Pailler, and J. L. Lamon, "Single‐and multilayered interphases in SiC/SiC composites exposed to severe environmental conditions: an overview," *International Journal of Applied Ceramic Technology,* 7[3] 263-75 (2010).
11. C. G. Cofer, A. W. Saak, and J. Economy, "Carbon/Boron Nitride Composites: An Alternative to Carbon/Carbon,″ pp. 663-71 in Proceedings of the 19th Annual Conference on Composites, Advanced Ceramics, Materials, and Structures—B: Ceramic Engineering and Science Proceedings. Vol. 16.
12. K. Shimoda and T. Hinoki, "Effect of BN nanoparticle content in SiC matrix on microstructure and mechanical properties of SiC/SiC composites," *International Journal of Applied Ceramic Technology* (2023).
13. R. H. Baughman, A. A. Zakhidov, and W. A. de Heer, "Carbon Nanotubes--the Route Toward Applications," *Science,* 297[5582] 787-92 (2002).
14. X. Ding, D. He, L. Yin, N. Zhang, H. Zhao, and J. Bai, "The synergistic improvement in mechanical strength and toughness obtained in epoxy-based composites incorporating with carbon nanotubes-polymer hybrid construction," *Journal of Applied Polymer Science,* 140[22] e53920 (2023).
15. T. Yamabe and K. Fukui., "The Science and Technology of Carbon Nanotubes,″ pp. 639-40 Vol. 8. Elsevier (1999).
16. Y. Liu, D. He, A.-L. Hamon, B. Fan, P. Haghi-Ashtiani, T. Reiss, and J. Bai, "Comparison of different surface treatments of carbon fibers used as reinforcements in epoxy composites: Interfacial strength measurements by in-situ scanning electron microscope tensile tests," *Composites Science and Technology,* 167 331-38 (2018).
17. X. Zhou, J. Yu, K. Sun, and S. Zhao, "In-situ grown carbon nanotubes and their applications for SiCf/SiC composites," *Chinese Journal of Nonferrous Metals,* 21[10] 2650-58 (2011).

18. V. P. Veedu, A. Cao, X. Li, K. Ma, C. Soldano, S. Kar, P. M. Ajayan, and M. N. Ghasemi-Nejhad, "Multifunctional composites using reinforced laminae with carbon-nanotube forests," *Nature Materials,* 5[6] 457-62 (2006).
19. S. Zhao, Z. Yang, X. Zhou, and K. Sun, "Fabrication and characterization of in-situ grown carbon nanotubes reinforced SiC/SiC composite," *Ceramics International,* 42[7] 9264-69 (2016).
20. K. Sun, J. Yu, C. Zhang, and X. Zhou, "In situ growth carbon nanotube reinforced SiCf/SiC composite," *Materials Letters,* 66[1] 92-95 (2012).
21. C. Zhen, X. Li, B. Zhang, X. Zhou, C. Liu, Z. Li, Y. Jiang, L. Zhang, and L. Cheng, "The improvement of mechanical properties of SiC/SiC composites by in situ introducing vertically aligned carbon nanotubes on the PyC interface," *Ceramics International,* 45[3] 3368-76 (2019).
22. S. Zhao, X. Zhou, J. Yu, and P. Mummery, "Mechanical properties and in situ crack growth observation of SiC/SiC composites," *Ceramics International,* 40[5] 7481-85 (2014).
23. X. Lue, L. Li, J. Sun, J. Yang, and J. Jiao, "Microstructure and tensile behavior of (BN/SiC)n coated SiC fibers and SiC/ SiC minicomposites," *Journal of the European Ceramic Society,* 43[5] 1828-42 (2023).
24. L. Li, "Synergistic effects of interface slip and fiber fracture on stress-dependent mechanical hysteresis of SiC/SiC minicomposites," *Composite Interfaces,* 27[10] 937-51 (2020).
25. Q. Wu, M. Li, Y. Gu, Y. Li, and Z. Zhang, "Nano-analysis on the structure and chemical composition of the interphase region in carbon fiber composite," *Composites Part a-Applied Science and Manufacturing,* 56 143-49 (2014).
26. J. Yang, F. Ye, and L. Cheng, "In-situ formation of Ti3SiC2 interphase in SiCf/SiC composites by molten salt synthesis," *Journal of the European Ceramic Society,* 42[4] 1197-207 (2022).
27. Z. Lu, Z. Qi, J. Yang, H. Liu, and J. Jiao, "The wetting‐to‐nonwetting transition of CVD BN coatings deposited at different temperatures," *International Journal of Applied Ceramic Technology* 1-9 (2023).
28. W. Cho, M. Schulz, and V. Shanov, "Growth and characterization of vertically aligned centimeter long CNT arrays," *Carbon,* 72 264-73 (2014).
29. S. W. Yoon, S. Y. Kim, J. Park, C. J. Park, and C. J. Lee, "Electronic Structure and Field Emission of Multiwalled Carbon Nanotubes Depending on Growth Temperature," *The Journal of Physical Chemistry B,* 109[43] 20403-06 (2005).
30. S. Agarwal, Q. Chen, T. Koyanagi, Y. Zhao, S. J. Zinkle, and W. J. Weber, "Revealing irradiation damage along with the entire damage range in ion-irradiated SiC/SiC composites using Raman spectroscopy," *Journal of Nuclear Materials,* 526 151778 (2019).
31. Y. Mu, W. Zhou, F. Luo, and D. Zhu, "Effects of BN/SiC dual-layer interphase on mechanical and dielectric properties of SiCf/SiC composites," *Ceramics International,* 40[2] 3411-18 (2014).
32. L. Song, L. Ci, H. Lu, P. B. Sorokin, C. Jin, J. Ni, A. G. Kvashnin, D. G. Kvashnin, J. Lou, and B. I. Yakobson, "Large scale growth and characterization of atomic hexagonal boron nitride layers," *Nano letters,* 10[8] 3209-15 (2010).
33. L. Charpentier, K. Dawi, M. Balat-Pichelin, E. Bêche, and F. Audubert, "Chemical degradation of SiC/SiC composite for the cladding of gas-cooled fast reactor in case of severe accident scenarios," *Corrosion science,* 59 127-35 (2012).
34. Y. Jiao, Q. Song, X. Yin, L. Han, W. Li, and H. Li, "Grow defect-rich bamboo-like carbon nanotubes on carbon black for enhanced microwave absorption properties in X band," *Journal of Materials Science & Technology,* 119 200-08 (2022).
35. B. P. Swain, "The analysis of carbon bonding environment in HWCVD deposited a-SiC: H films by XPS and Raman spectroscopy," *Surface and Coatings Technology,* 201[3-4] 1589-93 (2006).

36. K. Kim and J. Kim, "Fabrication of thermally conductive composite with surface modified boron nitride by epoxy wetting method," *Ceramics International,* 40[4] 5181-89 (2014).
37. F. S. Boi, J. Guo, S. Wang, Y. He, G. Xiang, X. Zhang, and M. Baxendale, "Fabrication of cm scale buckypapers of horizontally aligned multiwalled carbon nanotubes highly filled with Fe 3 C: The key roles of Cl and Ar-flow rates," *Chemical Communications,* 52[22] 4195-98 (2016).
38. S. Herreyre, P. Gadelle, P. Moral, and J. Millet, "Study by Mössbauer spectroscopy and magnetization measurement of the evolution of iron catalysts used in the disproportionation of CO," *Journal of Physics and Chemistry of Solids,* 58[10] 1539-45 (1997).
39. L.-Y. Wang, R.-Y. Luo, G.-y. Cui, and Z.-f. Chen, "Oxidation resistance of SiCf/SiC composites with a PyC/SiC multilayer interface at 500° C to 1100° C," *Corrosion Science,* 167 108522 (2020).
40. N. Al Nasiri, N. Patra, N. Ni, D. D. Jayaseelan, and W. E. Lee, "Oxidation behaviour of SiC/SiC ceramic matrix composites in air," *Journal of the European Ceramic Society,* 36[14] 3293-302 (2016).
41. D. He, "Formation of hybrid structures of carbon nanotubes and alumina microparticles by CVD method: Mechanisms and Chemical kinetics." in. Ecole Centrale Paris, 2010.
42. R. Baker, "Catalytic growth of carbon filaments," *Carbon,* 27[3] 315-23 (1989).
43. H. Plaisantin, S. Jacques, J. Danet, G. Camus, and H. Delpouve, "TEM characterization of turbostratic and rhombohedral BN interphases synthesized by chemical vapour infiltration in SiC/SiC-Si composites," *Materials Characterization,* 172 110857 (2021).
44. D. L. Poerschke, M. N. Rossol, and F. W. Zok, "Intermediate temperature internal oxidation of a SiC/SiCN composite with a polymer‐derived matrix," *Journal of the American Ceramic Society,* 99[9] 3120-28 (2016).
45. F. Rebillat, E. Garitte, and A. Guette, "Quantification of Higher SiC Fiber Oxidation Rates in Presence of B2O3 Under Air," *Design, Development, and Applications of Engineering Ceramics and Composites: Ceramic Transactions,* 215 135-49 (2010).
46. J. Bonhomme, A. Argüelles, J. Viña, and I. Viña, "Fractography and failure mechanisms in static mode I and mode II delamination testing of unidirectional carbon reinforced composites," *Polymer Testing,* 28[6] 612-17 (2009).
47. S. Jacques, A. Lopez-Marure, C. Vincent, H. Vincent, and J. Bouix, "SiC/SiC minicomposites with structure-graded BN interphases," *Journal of the European Ceramic Society,* 20[12] 1929-38 (2000).

Fig.1 Schematic diagram of the fabrication procedures for SiC_f-CNTs/SiC, SiC_f@BN/SiC, and SiC_f@BN-CNTs/SiC composites.

Fig.2 Characterizations of the as-received SiC_f and SiC_f@BN; (a) SEM image of SiC_f; (b) EDS analysis of SiC_f; (c) SEM image of SiC_f@BN; (d) EDS of SiC_f@BN

Fig.3 SEM images of SiC_f-CNTs (a-c) and SiC_f@BN-CNTs (d-f).

Fig.4 (a), XRD patterns of SiC_f, SiC_f@BN, and SiC_f@BN-CNTs ; (b), TGA of SiC_f@BN and SiC_f@BN-CNTs; (c-e), Raman spectra for samples in 800-2000 cm^{-1}.

Fig.5 XPS patterns for samples; XPS C 1s (a) and Si 2p (b) spectrum of SiC_f; wide scan XPS pattern (c) and B 1s spectrum (d) of SiC_f@BN; Wide scan XPS pattern (e) and C1s spectrum (f) of SiC_f@BN-CNTs.

Fig.6 TEM images of SiC_f-CNTs/SiC composites, low magnification morphology, (a-b); HRTEM images of SiC_f bound region with the interface (c), the interface (d), the interface bound region with SiC_m (e) and the SiC_m (f); HRTEM and SAED images of SiC_f@BN/SiC composites, (g): SiC_f; (h): the interface; (i): the Fe particle; (j): SiC_m.

Fig.7 EDS spectrum of SiC_f-CNTs/SiC composites; the mapping of elements (a); histogram of the percentage of each element in different regions, (b) atomic fraction; (c) weight fraction.

Fig.8 TEM images of SiC_f@BN/SiC composites, low magnification morphology (a); HRTEM images of SiC_f bound region with BN (b) and BN bound region with SiC_m (c); HRTEM and SAED images of SiC_f@BN/SiC composites, (d): SiC_f; (e): BN; (f): SiC_m.

Fig.9 EDS spectrum of SiC_f@BN/SiC composites; the mapping of elements (a); histogram of the percentage of each element in different regions, (b) atomic fraction; (c) weight fraction.

Fig.10 TEM images of SiC_f@BN-CNTs/SiC composites, low magnification morphology, (a-b); HRTEM images of SiC_f bound region with the interface (c), the interface bound region with SiC_m (d), and the SiC_m (e-f)； HRTEM and SAED images of SiC_f@BN/SiC composites, (g): SiC_f; (h): BN; (i): the enriched carbon; (j-k): Fe particles and CNTs; (l): SiC_m.

Fig.11 EDS spectrum of SiC_f@BN-CNTs/SiC composites; the mapping of elements (a); histogram of the percentage of each element in different regions, (b) atomic fraction; (c) weight fraction.

Fig.12 Mechanical properties; (a), Tensile fracture strength; (b), Ultimate tensile strain.

Fig.13 Fracture surface of SiC_f-CNTs/SiC (a-c), SiC_f@BN/SiC (d-f), and SiC_f@BN-CNTs/SiC (g-l).